nanomaterials

MDPI

Article

LDH/MXene Synergistic Carrier Separation Effects to Improve the Photoelectric Catalytic Activities of Bi_2WO_6 Nanosheet Arrays

Yuting Wang †, Runhua Li †, Jiaying Zhang, Liming Liu, Weiwei Huang and Yajun Wang *

State Key Laboratory of Heavy Oil Processing, China University of Petroleum, Beijing 102249, China; wangyt@cup.edu.cn (Y.W.); 2021215954@student.cup.edu.cn (R.L.); 2020211160@student.cup.edu.cn (J.Z.); 2021211158@student.cup.edu.cn (L.L.); 2022211152@student.cup.edu.cn (W.H.)

* Correspondence: wangyajun@cup.edu.cn

† These authors contributed equally to this work.

Abstract: Photoelectric catalysis is a green and efficient way to degrade pollutants, which has been paid more and more attention by researchers. Among them, Bi_2WO_3 has been proved to have excellent photocatalytic oxidation activity on its {001} facets. In this study, {001}-oriented facets with high exposure were successfully integrated into Bi_2WO_6 nanoplate arrays (Bi_2WO_6 NAs) to create a photoelectrode. This structure was grown in situ on an indium tin oxide (ITO) substrate. To promote photogenerated carrier separation efficiency and reduce agglomeration of Bi_2WO_6 photocatalysts, the electrochemical deposition of NiFe–layered double hydroxide (NiFe-LDH) and Ti_3C_2 (MXene) were introduced in this research to synergistically catalyze pollutant degradation. Morphology, spectral characterization, and electrochemical analysis jointly confirmed that the outstanding performance of hole capture behavior with LDH and electron conduction properties with MXene were the main reasons for the improvement in catalytic activity of the photoelectrode. Taking bisphenol A (BPA) as the model pollutant, the rate constant k of the NiFe-LDH/Ti_3C_2/Bi_2WO_6 NAs photoelectrode reaches 0.00196 min^{-1} under photoelectrocatalytic (PEC) conditions, which is 4.5 times that of the pure Bi_2WO_6 NAs photoelectrode. This work provides a new way to improve the reaction kinetics of the PEC degradation of pollutants.

Keywords: Bi_2WO_6; MXene; NiFe-LDH; photoelectrocatalytic; bisphenol A

Citation: Wang, Y.; Li, R.; Zhang, J.; Liu, L.; Huang, W.; Wang, Y. LDH/MXene Synergistic Carrier Separation Effects to Improve the Photoelectric Catalytic Activities of Bi_2WO_6 Nanosheet Arrays. *Nanomaterials* **2024**, *14*, 477. https://doi.org/10.3390/nano14050477

Academic Editor: Diana Sannino

Received: 31 January 2024
Revised: 23 February 2024
Accepted: 5 March 2024
Published: 6 March 2024

1. Introduction

Photoelectrocatalysis, as a green way to solve water pollution, has the advantages of electrocatalytic (EC) and photocatalytic (PC) oxidation [1,2]. During the photoelectrocatalytic (PEC) process, photogenerated electrons are driven towards the counter electrode by an external potential. This mechanism facilitates the efficient separation of photogenerated electrons and holes, thereby significantly enhancing photocatalytic activity [3–6].

As a significant semiconductor photocatalytic material, Bi_2WO_6 is the simplest compound in the Aurivillius family, which is alternately composed of $[Bi_2O_2]^{2+}$ layers and perovskite-like $(WO_4)^{2-}$ octahedral layers, and is widely used in PEC oxidation [3,7]. As a narrow band gap semiconductor (2.75 eV), Bi_2WO_6 has the advantages of a non-toxic, high-stability, and visible-light response [8–10]. Nevertheless, this material exhibits certain drawbacks, such as a high rate of electron and hole recombination, a low specific surface area, and a tendency towards easy agglomeration [4,11,12]. In order to address these issues, a variety of strategies have been employed to improve the photocatalytic performance of Bi_2WO_6. These methods include doping, the construction of heterojunctions, and surface hybridization [8,13–15]. In 2005, Zhu and co-workers synthesized Bi_2WO_6 nanostructures for the first time through simple hydrothermal treatment, which set a precedent for the preparation of Bi_2WO_6 nanostructures [16]. Cao and co-workers successfully prepared the

2D/2D heterojunction of ultra-thin Ti_3C_2/Bi_2WO_6 nanosheets, which have a short charge transfer distance and large interface contact area. Under simulated solar light irradiation, the combined yield of CH_4 and CH_3OH achieved by the Ti_3C_2/Bi_2WO_6 composite is 4.6 times higher than that of pure Bi_2WO_6 in the CO_2 reduction reaction [17].

Layered double hydroxide (LDH) is a type of layered inorganic functional material, characterized by a positively charged layer and an anion that is exchangeable in the interlayer space [18–20]. LDH has attracted much attention due to its unique layered structure and exchangeable anion between layers [21,22]. In recent years, Zhu et al. reported three-dimensional $BiVO_4$/NiFe-LDH heterostructures. The combination of $BiVO_4$ and NiFe-LDH can accelerate photogenerated charge separation and photoelectrocatalytic activity [23]. Zhang and colleagues synthesized a ZnCr–CO_3LDH/ruptured tubular g-C_3N_4 photocatalyst and observed that its capability to separate electron–hole pairs was enhanced by approximately fivefold and twofold, respectively, compared to bulk g-C3N4 and ruptured tubular g-C_3N_4 [24]. MXenes, a novel class of two-dimensional (2D) layered materials, are composed of transition metal carbides or carbonitrides. The general formula for MXenes is $M_{n+1}X_n$ (where n = 1, 2, or 3), with 'M' representing a transition metal (such as Sc, Ti, Zr, Hf, V, Nb, Ta, or Mo), and 'X' denoting carbon (C) and/or nitrogen (N). Notably, MXenes (Ti_3C_2), synthesized by selectively etching out the 'A' layers from Ti_3AC_2 (where 'A' can be Al, Zn, Si, or Ga), have become a focal point in research on the synthesis of MXene-based photocatalysts [25,26]. It is mainly attributed to the following excellent properties of Ti_3C_2: (i) The Ti_3C_2 surface of MXenes, adorned with various terminal functional groups such as -OH, -O, and -F, can establish a strong chemical interface with semiconductors [27]. This interaction significantly contributes to inhibiting the recombination of electrons and holes [17]. (ii) The notable metallic conductivity of Ti_3C_2 ensures rapid carrier migration, thereby facilitating efficient separation of electrons and holes [28,29]. (iii) The exposed terminal metal sites on Ti_3C_2 are likely to result in higher reactivity compared to that of carbon-based materials [26,30]. Given the aforementioned characteristics, Ti_3C_2 has emerged as a favored co-catalyst in the synthesis of photocatalysts [31]. Li et al. reported that mesoporous TiO_2 nanoparticles were successfully anchored onto a highly conductive Ti_3C_2 MXene co-catalyst using an electrostatic self-assembly strategy. The composite material, TiO_2/Ti_3C_2, has demonstrated superior photocatalytic performance. This is particularly evident in its ability to degrade methyl orange, where it achieved an exceptionally high efficiency of 99.6%. Additionally, the material exhibits a significant hydrogen production rate, quantified at 218.85 $\mu mol \cdot g^{-1} \cdot h^{-1}$. These findings underscore the composite's potential efficacy in photocatalytic applications [32]. Ran et al. synthesized Ti_3C_2 nanoparticles with CdS to induce a photocatalytic hydrogen production activity of 14,342 $\mu mol \cdot g^{-1} \cdot h^{-1}$. The enhanced performance observed can be attributed to the advantageous characteristics of the Ti_3C_2 nanoparticles. Specifically, favorable positioning of the Fermi level, coupled with the nanoparticles' excellent electrical conductivity, play critical roles in facilitating the high efficiency of the composite. These properties significantly contribute to the overall superior photocatalytic performance of the material [28].

In this work, we synthesized a Bi_2WO_6 photoelectrode with a large proportional exposure of {001} facets on an ITO substrate in situ (Bi_2WO_6 NAs). Subsequently, the NiFe-LDH/Ti_3C_2/Bi_2WO_6 NAs photoelectrode was synthesized via electrochemical deposition, layering NiFe-LDH and delaminating Ti_3C_2 onto Bi_2WO_6 NAs. Delaminated MXenes were utilized due to their superior electrical conductivity and robust mechanical properties, which are essential for the photocatalytic applications investigated. The layered structure facilitates efficient electron transport and provides numerous active sites for photocatalytic reactions, thereby enhancing the overall performance of the photocatalysts. This approach ensured precise material integration for the composite electrode. Taking the degradation of bisphenol A (BPA) as an example, the effect of the combination of Ti_3C_2 and NiFe-LDH on the catalytic performance of the Bi_2WO_6 NAs photoelectrode was investigated. Under PC, EC, and PEC conditions, the degradation activity of the NiFe-LDH/Ti_3C_2/Bi_2WO_6 NAs photoelectrode is better than that of the Bi_2WO_6 NAs photoelectrode, and the or-

der of activity from high to low is NiFe-LDH/Ti_3C_2/Bi_2WO_6 NAs > NiFe-LDH/Bi_2WO_6 NAs > Ti_3C_2/Bi_2WO_6 NAs > Bi_2WO_6 NAs. The extensive exposure of {001} facets in the Bi_2WO_6 nanoplate arrays (NAs) photoelectrode is advantageous for photocatalytic oxidation reactions. Moreover, the synergistic interaction between NiFe–layered double hydroxide (LDH) and Ti_3C_2 significantly enhances the separation efficiency of photogenerated carriers in Bi_2WO_6. Performance of the NiFe-LDH/Bi_2WO_6 photoelectrode and the mechanism of enhancing its PEC activity have been systematically studied.

2. Results and Discussion

2.1. Catalyst Characterization

The crystallographic structure and compositional analysis of the synthesized samples were examined utilizing X-ray diffraction (XRD) techniques. (Figure 1a). The XRD pattern shows three diffraction peaks at 8.9°, 18.3°, and 60.8°, corresponding to the (002), (004), and (110) planes of Ti_3C_2, respectively [29]. In addition, all of the diffraction peaks match well with the Bi_2WO_6 NAs according to JCPDS 39-0256 [33]. The observed intensity ratio of the {002} and {131} peaks in Bi_2WO_6 nanoplate arrays (NAs) is approximately 0.5, which is notably higher than the standard value of 0.19. This indicates that the as-prepared Bi_2WO_6 NAs exhibit anisotropic growth along the {001} planes. The extensive exposure of {001}-oriented Bi_2WO_6 NAs is advantageous, as it facilitates photocatalytic oxidation reactions [34]. After adding Ti_3C_2 (MXene) in the formation of Bi_2WO_6 NAs, the area integral ratio of diffraction peak between {002} and {131} crystal planes increases to 0.54, indicating that the existence of MXene expanded the {001}-orientated crystal faces exposure of Bi_2WO_6 NAs. The observed negativity of the Ti_3C_2 surface can be attributed to the adsorption of a substantial quantity of -F and -OH groups. This characteristic is particularly relevant during the preparation of MXene, where Bi^{3+} ions are adsorbed onto the Ti_3C_2 surface, further influencing its chemical behavior and interactions. Therefore, Bi_2WO_6 NAs expose more $[Bi_2O_2]^{2+}$ layers parallel to the {001} crystal plane. In addition, the diffraction peak of Bi_2WO_6 NAs becomes wider, which is due to the growth-limiting effect of MXene on Bi_2WO_6 NAs [17]. UV-Vis Diffuse Reflectance Spectroscopy (DRS) spectra provide insights into the optical properties of the as-prepared samples. As shown in Figure 1b, Bi_2WO_6 NAs, NiFe-LDH/Bi_2WO_6 NAs, Ti_3C_2/Bi_2WO_6 NAs, and NiFe-LDH/Ti_3C_2/Bi_2WO_6 NAs photoelectrodes have obvious absorption responses in the visible light region. Moreover, the absorption edge of Ti_3C_2/Bi_2WO_6 NAs and NiFe-LDH/Ti_3C_2/Bi_2WO_6 NAs photoelectrodes is near 450 nm, indicating that the combination of Ti_3C_2 broadens the response of Bi_2WO_6 NAs to visible light.

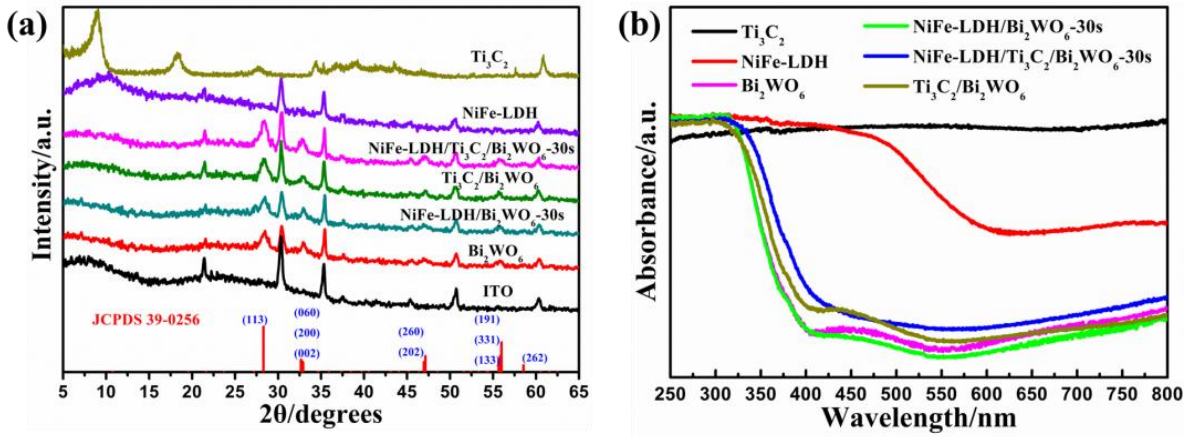

Figure 1. (**a**) XRD patterns of ITO, NiFe-LDH, Ti_3C_2, Bi_2WO_6 NAs, NiFe-LDH/Bi_2WO_6 NAs, Ti_3C_2/Bi_2WO_6 NAs, and NiFe-LDH/Ti_3C_2/Bi_2WO_6 NAs; (**b**) UV-Vis DRS spectra of NiFe-LDH, Ti_3C_2, Bi_2WO_6 NAs, NiFe-LDH/Bi_2WO_6 NAs, Ti_3C_2/Bi_2WO_6 NAs, and NiFe-LDH/Ti_3C_2/Bi_2WO_6 NAs.

Scanning electron microscopy (SEM) images (Figures 2a and S1) exhibit that Bi_2WO_6 nanosheets are vertically grown on the ITO substrate with a size of about 200 nm. The nanoplates are interconnected, forming a framework array structure. Following compounding with Ti_3C_2, the size of Bi_2WO_6 nanosheets is observed to be approximately 100 nm. This dimension is attributed to the growth restriction imposed by Ti_3C_2 on Bi_2WO_6. (Figure 2b,c) [17]. Figure 2d displays the structural morphology of the NiFe–layered double hydroxide (LDH)/Ti_3C_2/Bi_2WO_6 nanoplate arrays (NAs) photoelectrode. NiFe-LDH is observed to be uniformly coated on the Ti_3C_2/Bi_2WO_6 surface, presenting a flocculent morphology that is evenly dispersed. As shown in Supplementary Figure S2, the uniform detection of elements such as tungsten (W), bismuth (Bi), oxygen (O), nickel (Ni), iron (Fe), titanium (Ti), and carbon (C) confirms the even distribution of NiFe-LDH and Ti_3C_2 across the Bi_2WO_6 NAs.

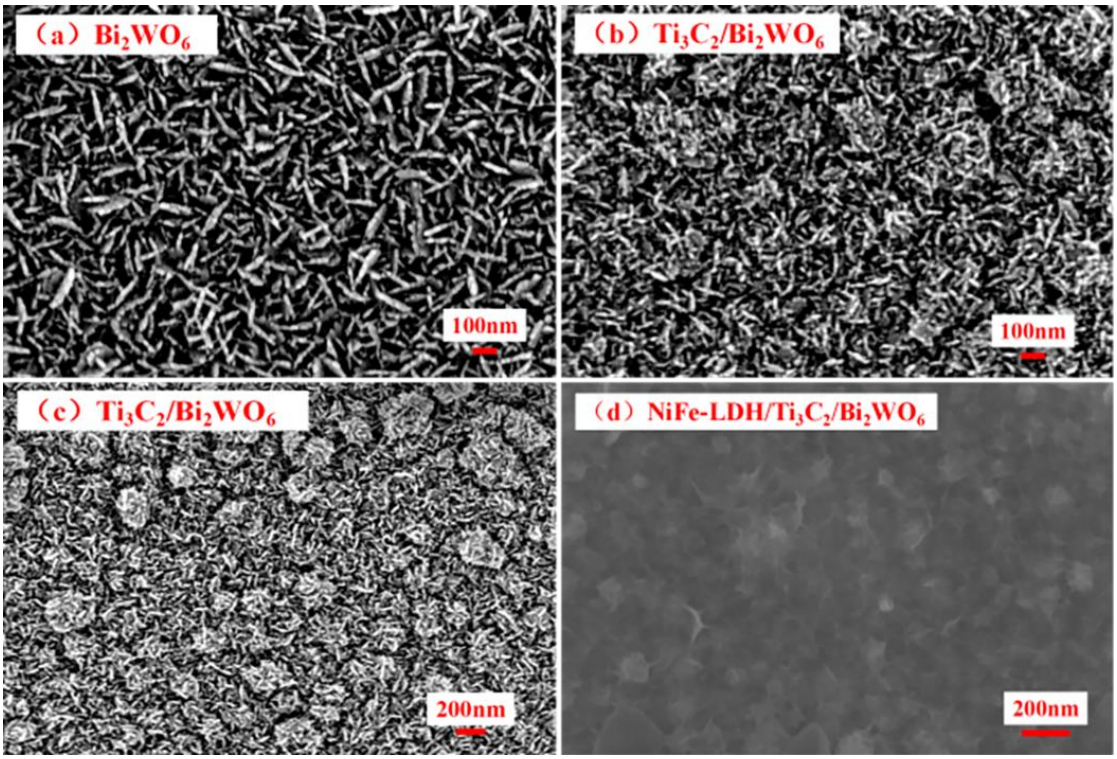

Figure 2. SEM images of (**a**) Bi_2WO_6 NAs; (**b**,**c**) Ti_3C_2/Bi_2WO_6 NAs; (**d**) NiFe-LDH/Ti_3C_2/Bi_2WO_6 NAs.

2.2. Enhanced PEC Degradation Activity

Catalytic performance of as-prepared catalysts is estimated by the degradation of BPA in aqueous solution under PC, EC, and PEC systems. As can be seen from Figure S3, BPA does not undergo self-degradation under visible light irradiation. The EC activity of the Bi_2WO_6 NAs photoelectrode also shows a low degradation rate of BPA (Figures 3a and 4a). Generally speaking, Ti_3C_2 and NiFe-LDH are excellent electrocatalytic materials with high conductivity, so the EC activity is significantly improved after compounding with Ti_3C_2 and NiFe-LDH. Upon exposure exclusively to visible light, the degradation rate constant, denoted as k, of the NiFe-LDH/Ti_3C_2/Bi_2WO_6 nanocomposite photoelectrode exhibits an enhancement by a factor of approximately 10 compared to the degradation rate constant of the pristine Bi_2WO_6 nanocomposite photoelectrode (Figures 3b and 4b) due to the excellent electron transport properties of Ti_3C_2 and the fast trapping of photogenerated holes by NiFe-LDH. In the PEC system, the catalytic performance of Bi_2WO_6 NAs, Ti_3C_2/Bi_2WO_6 NAs, NiFe-LDH/Bi_2WO_6 NAs, and NiFe-LDH/Ti_3C_2/Bi_2WO_6 NAs photoelectrodes is further improved, all of which are higher than the PC or EC system alone (Figures 3c and 4c).

The external potential can quickly transfer the photogenerated electrons generated by Bi_2WO_6 NAs to the counter electrode through the external circuit. Consequently, PEC activity escalates with the augmentation of external potential. At external potentials below the water decomposition threshold, such potential facilitates the migration of electrons towards the counter electrode, thereby enhancing the segregation of photogenerated electrons and holes. Conversely, when the external potential surpasses the threshold for water decomposition, it instigates complex oxidation processes. Figure S4 shows the PEC performance of the NiFe-LDH/Ti_3C_2/Bi_2WO_6 NAs photoelectrode under different external potentials. Under the irradiation of visible light ($\lambda \geq 420$ nm), the PEC degradation rate of BPA gradually increases with increasing external potential. However, when the external potential reaches 3.0 V, the surface of the Bi_2WO_6 NAs photoelectrode blackens rapidly, leading to deactivation of the catalyst and a sharp decrease in degradation activity.

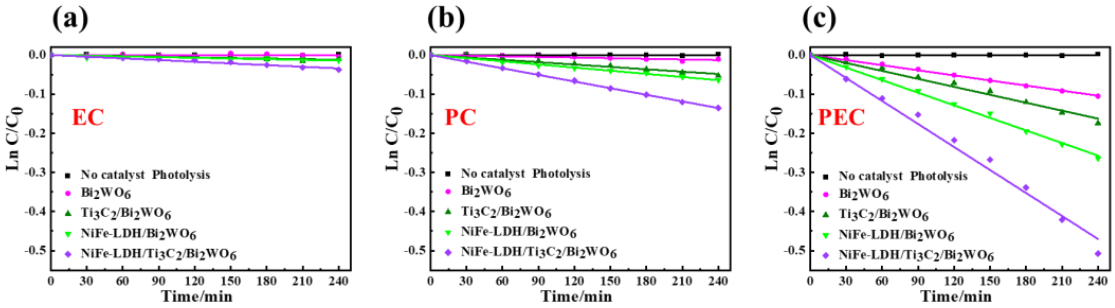

Figure 3. Comparison of (**a**) EC, (**b**) PC, and (**c**) PEC degradation over time, and its first-order reaction fitting curves over Bi_2WO_6 NAs, NiFe-LDH/Bi_2WO_6 NAs, Ti_3C_2/Bi_2WO_6 NAs, and NiFe-LDH/Ti_3C_2/Bi_2WO_6 NAs photoelectrodes ($\lambda \geq 420$ nm, external potential = 1.0 V). The associated rate constant, denoted as *k*.

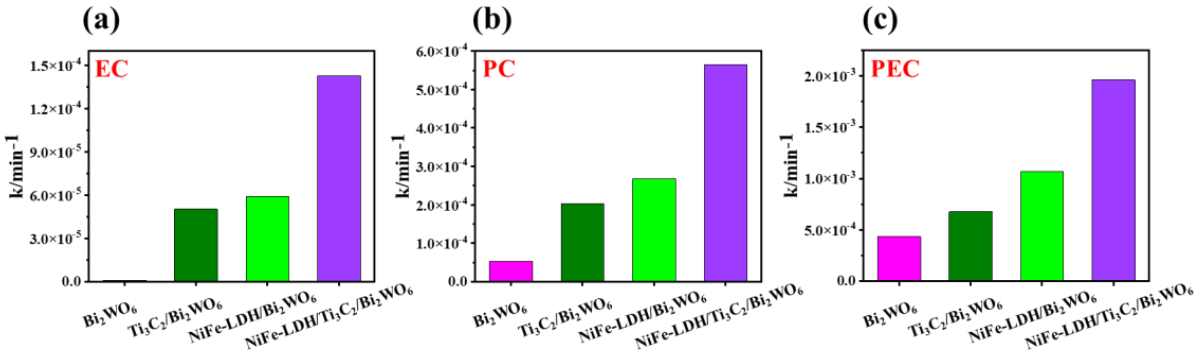

Figure 4. Comparison of (**a**) EC, (**b**) PC, and (**c**) PEC degradation rates over Bi_2WO_6 NAs, NiFe-LDH/Bi_2WO_6 NAs, Ti_3C_2/Bi_2WO_6 NAs, and NiFe-LDH/Ti_3C_2/Bi_2WO_6 NAs photoelectrodes.

2.3. Enhancement Mechanism of Photoelectrochemical (PEC) Activity

To elucidate the underlying mechanism behind the augmented PEC activity of NiFe-LDH/Ti_3C_2/Bi_2WO_6 nanocomposites, an array of photoelectrical characterizations has been conducted. As can be seen from Figure 5a, the photocurrent density of the NiFe-LDH/Ti_3C_2/Bi_2WO_6 NAs photoelectrode reaches about 3.0 $\mu A/cm^2$, which represents an enhancement of approximately 3.8-fold compared to the Ti_3C_2/Bi_2WO_6 nanocomposite photoelectrode and a 6.0-fold increase over the pristine Bi_2WO_6 nanocomposite photoelectrode. The increase of photocurrent density of the NiFe-LDH/Ti_3C_2/Bi_2WO_6 NAs photoelectrode is attributed to the synergistic effect of NiFe-LDH and Ti_3C_2, which greatly improves the separation efficiency of Bi_2WO_6 NAs photogenerated charge. Electrochemical impedance spectroscopy is utilized to investigate the impedance characteristics of the synthesized samples, as depicted in Figure 5b. The curve radius of the pure Bi_2WO_6 NAs

photoelectrode is the largest, and the impedance value is also the largest. After compounding with Ti_3C_2 and NiFe-LDH, the curve radius of the NiFe-LDH/Ti_3C_2/Bi_2WO_6 NAs photoelectrode decreases and the impedance value decreases accordingly, which is consistent with the above transient photocurrent response results. The catalytic performance of the as-prepared sample is investigated by linear sweep voltammetry (LSV) (Figure 5c). The order of current density under different external potentials is NiFe-LDH/Ti_3C_2/Bi_2WO_6 NAs > NiFe-LDH/Bi_2WO_6 NAs > Ti_3C_2/Bi_2WO_6 NAs > Bi_2WO_6 NAs. Furthermore, the starting potential of the NiFe-LDH/Ti_3C_2/Bi_2WO_6 NAs photoelectrode has an obvious negative shift, indicating that the NiFe-LDH/Ti_3C_2/Bi_2WO_6 NAs photoelectrode has a stronger redox ability. From Figure 5d, the curve slopes of the Bi_2WO_6 NAs, NiFe-LDH/Bi_2WO_6 NAs, Ti_3C_2/Bi_2WO_6 NAs, and NiFe-LDH/Ti_3C_2/Bi_2WO_6 NAs photoelectrodes are all positive, which demonstrates that Bi_2WO_6 is an N-type semiconductor. At the same time, after compounding with Ti_3C_2 and NiFe-LDH, the flat band potential shifts significantly, illustrating that the band edge bending of the NiFe-LDH/Ti_3C_2/Bi_2WO_6 NAs photoelectrode decreases. It is beneficial to promote charge transfer at the electrode/electrolyte interface, accelerate the surface reaction kinetics process, and then enhance catalytic performance. To investigate the correlation between the photoelectric properties and light absorption capabilities of the synthesized samples, the photoelectric conversion efficiency of Bi_2WO_6 NAs, NiFe-LDH/Bi_2WO_6 NAs, Ti_3C_2/Bi_2WO_6 NAs, and NiFe-LDH/Ti_3C_2/Bi_2WO_6 NAs photoelectrodes are calculated (Figure S5). All samples have a photoelectric conversion ability in the ultraviolet region, and the NiFe-LDH/Ti_3C_2/Bi_2WO_6 NAs photoelectrode has the strongest photoelectric conversion ability.

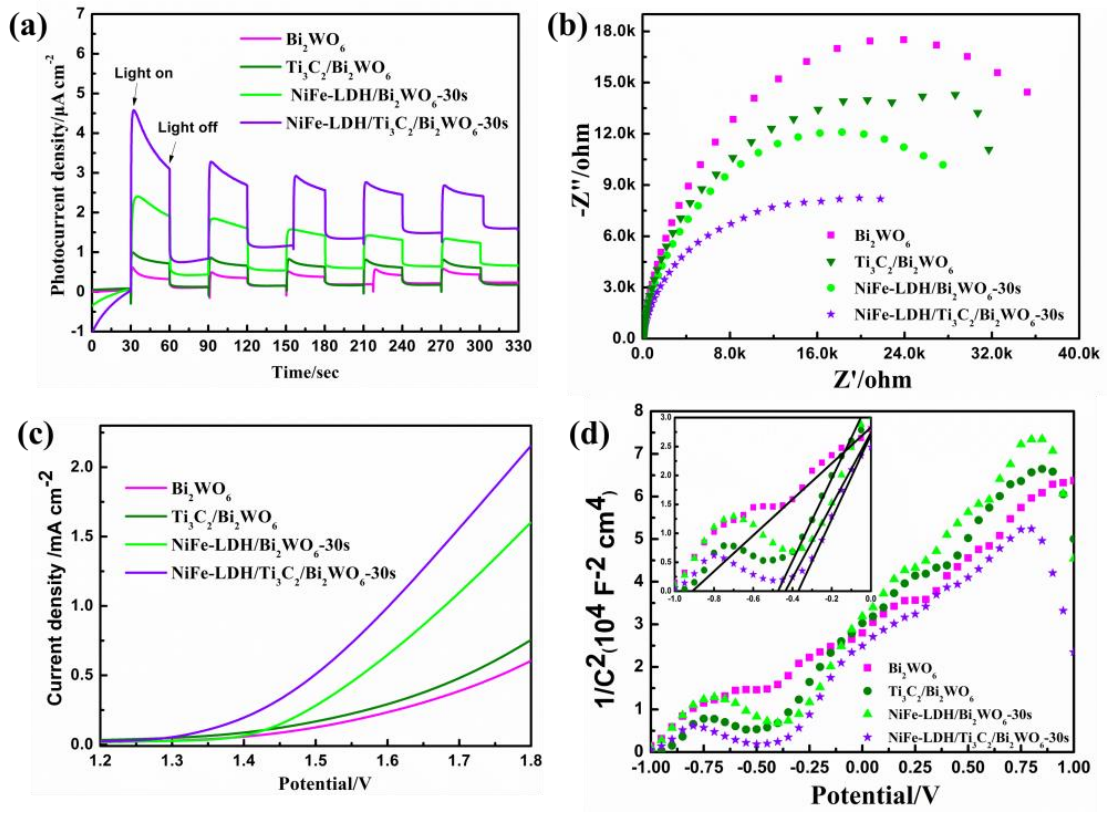

Figure 5. (**a**) Transient photocurrent density; (**b**) EIS Nyquist plots; (**c**) linear sweep voltammetry plots; (**d**) Mott–Schottky plots of Bi_2WO_6 NAs, NiFe-LDH/Bi_2WO_6 NAs, Ti_3C_2/Bi_2WO_6 NAs, and NiFe-LDH/Ti_3C_2/Bi_2WO_6 NAs ($\lambda \geq 420$ nm).

Figure 6 presents the outcomes of X-ray photoelectron spectroscopy (XPS) analyses performed on the catalysts. It was found that Bi, W, O, Ni, Fe, Ti, and C elements are present in the NiFe-LDH/Ti_3C_2/Bi_2WO_6 NAs photoelectrode (Figure 6a). Figure 6b illustrates the predominance of Ti-C bonds within the Ti2p peaks, alongside a minor presence of Ti-O structures. This suggests that while there may be slight oxidation of the Ti_3C_2 material, it does not detract from the dominant influence of the Ti_3C_2 structure in the ternary catalytic system. Figure 6c,d show the chemical states of Bi 4f and W 4f of as-prepared samples. Compared with that of Bi_2WO_6 NAs, the binding energy of Ti_3C_2/Bi_2WO_6 NAs in Bi 4f and W 4f spectra show positive shifts. However, the peak shifts of Bi 4f and Bi $4f_{5/2}$ in the NiFe-LDH/Bi_2WO_6 NAs photoelectrode are opposite [13,35]. Moreover, the O 1s spectra of the as-prepared sample in Figure 6e consists of Bi-O, W-O, and surface adsorbed oxygen [36]. The peak positions of Bi-O and W-O in the Ti_3C_2/Bi_2WO_6 NAs photoelectrode show positive shifts, and the position of adsorbed oxygen shifts to 531.78 eV. On the contrary, the peak positions of Bi-O and W-O in the NiFe-LDH/Bi_2WO_6 NAs photoelectrode shift negatively to 529.22 eV and 530.04 eV, and the peaks at 530.55 eV, 531.72 eV, and 532.30 eV belong to surface adsorbed oxygen, interlayer anion (OH^-), and H_2O of NiFe-LDH, respectively. The above proves that Bi_2WO_6 NAs interact with Ti_3C_2 and NiFe-LDH, respectively, inducing the migration of photogenerated electrons from Bi_2WO_6 NAs to Ti_3C_2 and photogenerated holes from Bi_2WO_6 NAs to NiFe-LDH. Furthermore, an upward shift in the peak positions of Ni 2p and Fe 2p observed in NiFe-LDH/Bi_2WO_6 nanocomposite photoelectrodes and NiFe-LDH/Ti_3C_2/Bi_2WO_6 nanocomposite photoelectrodes (as shown in Figure 6f,g) corroborates the interaction between the surface energy of Bi_2WO_6 nanocomposites and NiFe-LDH. This charge transfer mechanism aids in the efficient separation of electrons and holes, thereby improving photoelectrochemical performance.

Building on the preceding discussion, a more detailed mechanism is proposed for the photoelectrochemical (PEC) degradation of organic pollutants using the NiFe-LDH/Ti_3C_2/Bi_2WO_6 nanocomposite photoelectrode, as illustrated in Figure 7. The ternary composite system comprising Ti_3C_2, Bi_2WO_4, and layered double hydroxide (LDH) forms a unique and sophisticated heterojunction that exhibits characteristics of both Type-II and Z-scheme heterojunctions. This innovative configuration leverages the distinct electronic properties of each component to facilitate efficient charge separation and transfer, thereby enhancing photocatalytic performance under light irradiation. The Ti_3C_2/Bi_2WO_4 interface forms a Type-II heterojunction, where alignment of their conduction and valence bands allows for the spatial separation of photogenerated electrons and holes. Electrons tend to migrate towards Ti_3C_2, while holes accumulate in Bi_2WO_4, thus reducing the recombination rate and enhancing photocatalytic efficiency. The addition of LDH into the Ti_3C_2/Bi_2WO_4 system introduces a Z-scheme mechanism, particularly when LDH acts as a bridge for electron transfer between Ti_3C_2 and Bi_2WO_4. This configuration preserves the high reduction potential of Ti_3C_2's electrons and the high oxidation potential of Bi_2WO_4's holes, making the composite highly effective for redox reactions.

The LDH/Ti_3C_2/Bi_2WO_6 ternary composite system leverages a unique combination of Type-II and Z-scheme heterojunctions, offering significant advantages for photocatalytic applications. This sophisticated heterostructure ensures enhanced charge separation and transfer, effectively minimizing recombination and maximizing the availability of reactive charge carriers for photocatalysis. Additionally, the incorporation of these materials broadens the light absorption range, enabling the composite to utilize a larger portion of the solar spectrum, particularly under visible light, which significantly improves its photocatalytic activity. The Z-scheme configuration within this ternary system preserves the high reduction and oxidation potentials of electrons and holes, respectively, enabling the composite to efficiently participate in a wide range of redox reactions, including the degradation of pollutants and water splitting. Moreover, the synergistic effects among Ti_3C_2, Bi_2WO_4, and LDH not only enhance the composite's stability and durability under photocatalytic conditions but also ensure sustained activity over extended periods, making

the LDH/Ti_3C_2/Bi_2WO_6 system a highly efficient and versatile option for environmental remediation and energy conversion technologies.

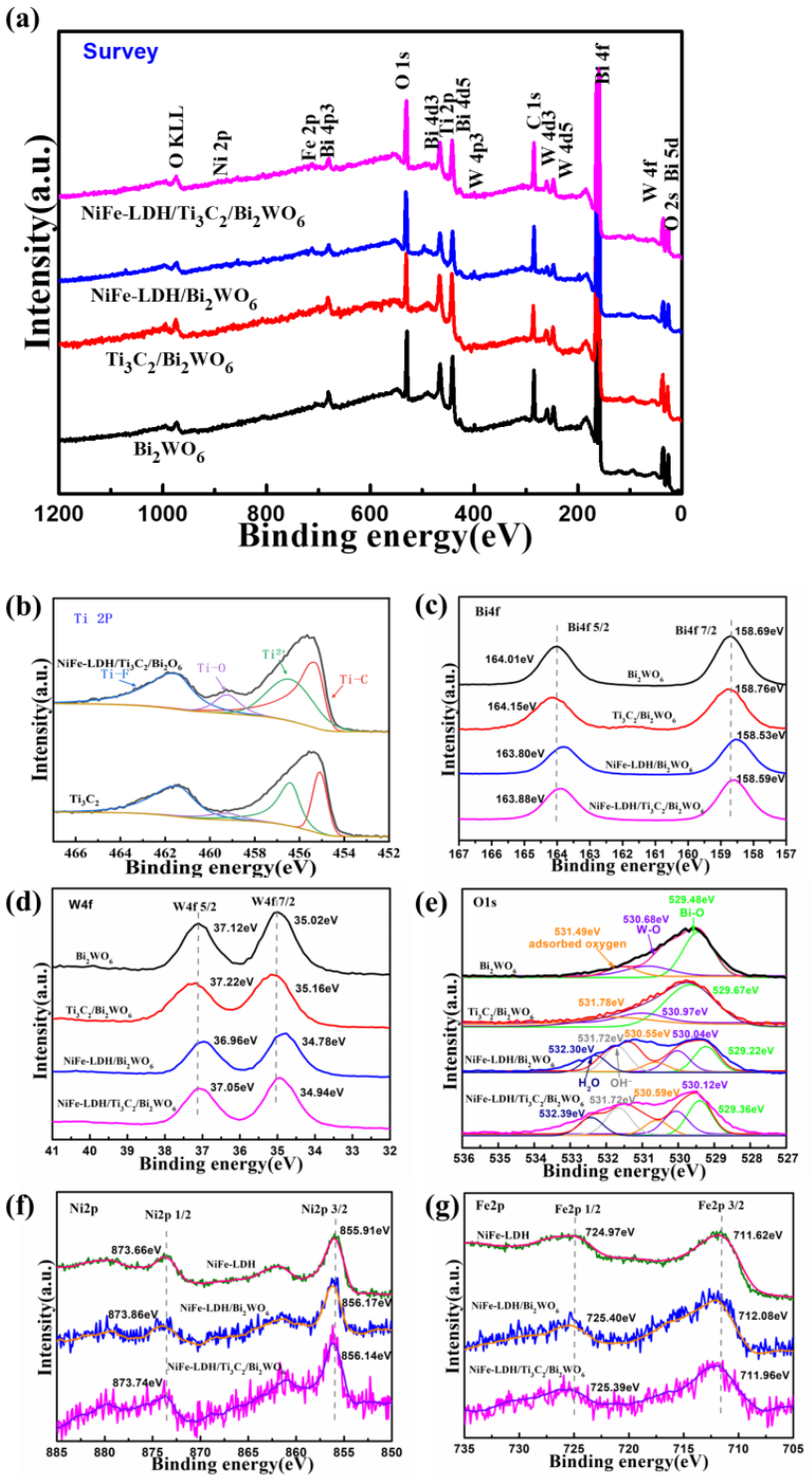

Figure 6. XPS of (**a**) survey spectra, (**b**) Ti 2p, (**c**) Bi 4f, (**d**) W 4f, (**e**) O 1s, (**f**) Ni 2p, and (**g**) Fe 2p of NiFe-LDH, Bi_2WO_6 NAs, NiFe-LDH/Bi_2WO_6 NAs, Ti_3C_2/Bi_2WO_6 NAs, and NiFe-LDH/Ti_3C_2/Bi_2WO_6 NAs.

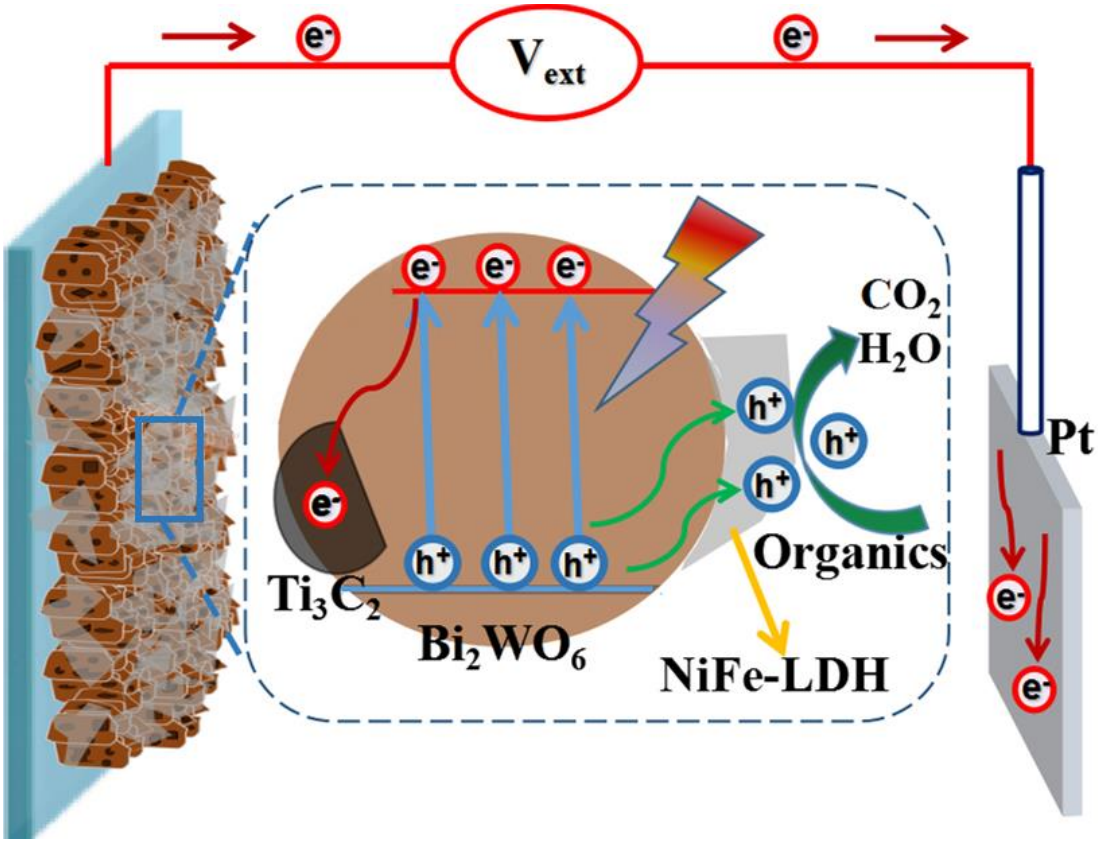

Figure 7. Schematic representation illustrating the photoelectrocatalytic degradation mechanism of organic compounds via the NiFe-LDH/Ti_3C_2/Bi_2WO_6 nanocomposite photoelectrode. This diagram delineates the process of photogenerated electron–hole pair separation and subsequent transfer, highlighting the synergistic effects of the composite materials in enhancing the degradation efficiency of organic pollutants (The red and green arrows indicate the direction of movement of electrons and holes, respectively).

The enhancement of PEC activity in this nanocomposite photoelectrode is the result of multiple synergistic effects, notably the following: (i) The enhanced exposure of {001} facets in Bi_2WO_6 nanocomposites within the NiFe-LDH/Ti_3C_2/Bi_2WO_6 framework significantly contributes to an increased generation of holes. This feature not only facilitates more active participation in the degradation process but also substantially strengthens photocatalytic oxidation reactions. The {001} facets of Bi_2WO_6 are known for their high photocatalytic activity, and their prominent exposure within the composite structure maximizes the photocatalytic sites available for reaction; (ii) The strategic integration of NiFe-LDH with Ti_3C_2 creates a highly effective conduit for the swift separation and transfer of photogenerated charges. Under illumination, the electrons excited from the conduction band of Bi_2WO_6 are quickly transferred to Ti_3C_2. This transition is facilitated by the close interfacing and strong electronic interaction between Bi_2WO_6 and Ti_3C_2, which serves as an effective conduit for the rapid transportation of electrons to the counter electrode via the external circuit. This bridging significantly curtails the recombination of photogenerated electron–hole pairs, thereby enhancing the overall separation efficiency of charge carriers; (iii) The directed migration of photogenerated holes towards the NiFe-LDH surface plays a crucial role in the oxidative degradation of organic pollutants. NiFe-LDH acts as a catalyst that accelerates the oxidation process, converting organic contaminants into carbon dioxide (CO_2) and water (H_2O). This process is facilitated by the high affinity of NiFe-LDH for photogenerated holes, which promotes their accumulation on the LDH surface, thereby increasing local hole concentration and enhancing the oxidation reaction rate. As a result, the NiFe-LDH/Ti_3C_2/Bi_2WO_6 nanocomposite photoelectrode represents a sophisticated integration

of materials that leverages the unique properties of each component to maximize PEC degradation efficiency. The optimized exposure of photocatalytically active facets, coupled with the strategic facilitation of charge separation and targeted reaction pathways, underpin the superior performance of this ternary composite in the PEC degradation of organic pollutants. This comprehensive understanding of the degradation mechanism provides valuable insights into designing more efficient PEC systems for environmental remediation.

3. Conclusions

In summary, the NiFe-LDH/Ti_3C_2/Bi_2WO_6 nanocomposite photoelectrode, featuring a significant proportion of {001}-oriented facets, was successfully synthesized through a solvothermal reaction followed by electrochemical deposition. Comparative analysis under electrochemical (EC), photocatalytic (PC), and photoelectrochemical (PEC) conditions revealed that the NiFe-LDH/Ti_3C_2/Bi_2WO_6 nanocomposite photoelectrode exhibits superior degradation performance relative to the pristine Bi_2WO_6 nanocomposite photoelectrode. The activity ranking, in descending order, is as follows: NiFe-LDH/Ti_3C_2/Bi_2WO_6 NAs > NiFe-LDH/Bi_2WO_6 NAs > Ti_3C_2/Bi_2WO_6 NAs > Bi_2WO_6 NAs. The augmented photocatalytic efficacy of the NiFe-LDH/Ti_3C_2/Bi_2WO_6 nanocomposite photoelectrode can be ascribed to the synergistic interplay between Ti_3C_2 and NiFe-LDH, which significantly enhances the charge separation efficiency and reaction kinetics of Bi_2WO_6 NAs. This study elucidates a novel approach for enhancing reaction kinetics in the PEC degradation of pollutants.

4. Materials and Methods

4.1. Preparation of Bi_2WO_6 NAs Photoelectrode

Initially, 0.9 g of polyvinylpyrrolidone (PVP) was dissolved in 30 mL of ethylene glycol at a temperature of 95 °C in two separate beakers to achieve a homogeneous, transparent solution. Subsequently, 0.3299 g of sodium tungstate dihydrate ($Na_2WO_4 \cdot 2H_2O$) was dissolved in the first beaker (hereafter referred to as solution 1), while 0.9701 g of bismuth nitrate pentahydrate ($Bi(NO_3)_3 \cdot 5H_2O$) was dissolved in the second beaker (referred to as solution 2). Solution 1 was then gradually introduced into solution 2 with constant stirring to ensure thorough mixing. The resultant mixture was subjected to a pre-reaction phase at 98 °C for 1.5 h with sustained stirring. Following this, the mixture was transferred into a Teflon-lined autoclave, in which cleaned indium tin oxide (ITO) substrates had been vertically positioned, and subsequently heated at 178 °C for 24 h. Upon cooling to ambient temperature, the ITO substrates were carefully removed, and washed multiple times with ethanol and deionized water to obtain the Bi_2WO_6 nanoplate arrays (NAs) photoelectrode.

4.2. Preparation of Ti_3C_2

A mass of 1.0 g of MAX phase powder (Ti_3AlC_2) was dispersed in a Teflon container. To this, 10 mL of 40% HF solution was added per gram of MAX phase, ensuring the mixture was stirred gently to achieve uniform etching. The reaction was allowed to proceed for 24 h at room temperature under constant stirring to facilitate the complete removal of the A layer. Following etching, the mixture was diluted with deionized water and allowed to settle, enabling the separation of undissolved solids. The supernatant, containing excess HF and reaction byproducts, was carefully decanted. This washing process was repeated several times until the pH of the supernatant reached neutrality, indicating the effective removal of residual HF. The resulting MXene was then collected by centrifugation at 3500 rpm for 5 min, washed with deionized water, and spread out for drying at room temperature in a fume hood or under vacuum at 60 °C. The dried MXene was stored in an airtight container under N_2 atmosphere to prevent oxidation.

4.3. Preparation of NiFe-LDH

A volume of 70 mL of deionized water was introduced into an electrolytic cell, followed by the addition of 0.15 mol of nickel nitrate hexahydrate ($Ni(NO_3)_2 \cdot 6H_2O$) and

0.15 mol of iron(II) sulfate heptahydrate ($FeSO_4 \cdot 7H_2O$). An indium tin oxide (ITO) substrate, a platinum wire, and an Ag/AgCl electrode were utilized as the working electrode, counter electrode, and reference electrode, respectively. The electrochemical deposition was conducted at a voltage of −1.0 V for a duration of 300 s. Subsequent to the electrochemical deposition, the ITO substrate was removed and exposed to ambient air to facilitate the natural oxidation of Fe^{2+} ions to Fe^{3+} ions. This process culminated in the formation of the NiFe–layered double hydroxide (LDH) electrode.

4.4. Preparation of Ti_3C_2/Bi_2WO_6 NAs Photoelectrode

Initially, 20 mL of ethylene glycol was introduced into two beakers, and subsequently placed in a 95 °C water bath. Nitrogen gas was infused into each beaker to establish an inert environment. To these, 0.6 g of polyvinylpyrrolidone (PVP) was added as a dispersant. Specifically, beaker 2 received 0.0093 g of Ti_3C_2 powder, with nitrogen flow maintained to protect the sensitive material. The mixture was sealed and magnetically stirred for 20 min, ensuring uniform dispersion of Ti_3C_2.

Simultaneously, 0.3299 g of $Na_2WO_4 \cdot 2H_2O$ and 0.9701 g of $Bi(NO_3)3 \cdot 5H_2O$ were added to beakers 1 and 2, respectively, under nitrogen to prevent any oxidative reactions. The contents of beaker 1 were slowly added to beaker 2, and the combined solution was pre-reacted for one hour at 95 °C, still under nitrogen. This mixture was then transferred to a 50 mL autoclave containing a pre-treated indium tin oxide (ITO) substrate, with the entire assembly purged with nitrogen. The autoclave underwent hydrothermal treatment at 180 °C for 24 h, facilitating formation of the composite on the ITO, all while under nitrogen to minimize degradation. Upon cooling to room temperature under nitrogen, the ITO substrate, coated with the Ti_3C_2/Bi_2WO_6 composite, was meticulously rinsed with deionized water and anhydrous ethanol, and dried in a vacuum oven at 60 °C.

4.5. Preparation of NiFe-LDH/Bi_2WO_6 NAs Photoelectrode

A volume of 70 mL of deionized water was added to an electrolytic cell. Then, under a nitrogen atmosphere and with continuous stirring, 0.15 M of $Ni(NO_3)2 \cdot 6H_2O$ and 0.15 M of $FeSO_4 \cdot 7H_2O$ were added, respectively. The flow of N_2 gas was to prevent the oxidation of Fe^{2+}. The electrochemical deposition of NiFe-LDH was carried out using a three-electrode system. A Bi_2WO_6 photoelectrode, a platinum wire, and an Ag/AgCl electrode were used as the working electrode, counter electrode, and reference electrode, respectively. The deposition voltage was set to −1.0 V, and the deposition time was 30 *s*. After the electrochemical deposition finished, the ITO was removed, rinsed with deionized water, and then placed in air to allow Fe^{2+} to naturally oxidize to Fe^{3+}. Finally, a NiFe-LDH/Bi_2WO_6 or NiFe-LDH/Ti_3C_2/Bi_2WO_6 composite photoelectrode was obtained.

4.6. Preparation of NiFe-LDH/Ti_3C_2/Bi_2WO_6 NAs Photoelectrode

A Ti_3C_2/Bi_2WO_6 NAs photoelectrode was used as the working electrode, and the experimental steps were repeated as in Section 4.5.

4.7. Characterization Techniques

X-ray diffraction (XRD) analyses were conducted using a Bruker D8-Focus diffractometer equipped with Cu Kα radiation. The morphology of the synthesized sample was examined via a scanning electron microscope (SEM, SU8010, Hitachi Ltd., Chiyoda, Japan) across an acceleration voltage range of 200 V to 30 kV, supplemented by energy dispersive X-ray (EDX) spectroscopy for elemental analysis. The interplanar spacing of the lattice fringes was determined using a high-resolution transmission electron microscope (HRTEM, Tecnai F20, FEI Company, Hillsboro, OR, USA). Ultraviolet-visible diffuse reflectance spectra (DRS) were acquired on a Hitachi 4100 spectrophotometer, employing $BaSO_4$ as the reference standard. X-ray photoelectron spectroscopy (XPS) measurements were performed on a PHI Quantera ULVAC XPS system (ULVAC, Inc., Chigasaki, Japan). Photoelectrocatalytic (PEC) characterizations were conducted in a quartz electrochemi-

cal cell, incorporating a three-electrode setup, with an electrochemical workstation (CHI 660D, CH Instruments, Inc., Shanghai, China). A 0.1 M solution of Na_2SO_4 served as the electrolyte. Electrochemical impedance spectroscopy (EIS) was executed over a frequency range from 0.005 Hz to 105 Hz, applying a sinusoidal AC disturbance signal of 5 mV to probe the electrochemical properties of the materials.

4.8. Degradation Activity Test

The PC and PEC activities of the synthesized samples were assessed through the degradation of bisphenol A (BPA) at a concentration of 10 mol·L^{-1} in a 50 mL solution of Na_2SO_4 (0.1 mol·L^{-1}). Prior to initiating the PC and PEC reactions, the solution was stirred in darkness for 30 min to establish adsorption–desorption equilibrium. For the PEC activity evaluation, a photoelectrode, a Pt wire, and a saturated calomel electrode (SCE) were employed as the working electrode, counter electrode, and reference electrode, respectively. The photoelectrode was exposed to either simulated sunlight or visible light ($\lambda > 420$ nm), generated by a 300 W Xe lamp (PLS-SXE300C/300CUV, Perfect Light Ltd, Beijing, China), with an average intensity of 100 mW cm^{-2}. For comparative analysis, the samples were also subjected to electrochemical (EC) degradation of BPA under identical conditions but without light irradiation. The degradation process was conducted over a duration of 4 h, with aliquots of 2.5 mL sampled every 30 min. The concentration of BPA was determined using a high-performance liquid chromatography (HPLC) system (Shimadzu LC-20AT, Shimadzu Corporation, Kyoto, Japan).

Supplementary Materials: The following supporting information can be downloaded at https://www.mdpi.com/article/10.3390/nano14050477/s1: Figure S1. SEM image of Bi_2WO_6 NAs; Figure S2. EDX mapping of NiFe-LDH/Ti_3C_2/Bi_2WO_6 NAs; Figure S3. Comparison of EC, PC, and PEC degradation rates over Bi_2WO_6 NAs, NiFe-LDH/Bi_2WO_6 NAs, Ti_3C_2/Bi_2WO_6 NAs, and NiFe-LDH/Ti_3C_2/Bi_2WO_6 NAs ($\lambda \geq 420$ nm, external potential = 1.0 V); Figure S4. Comparison of the PEC degradation rate of BPA over NiFe-LDH/Ti_3C_2/Bi_2WO_6 NAs at different bias voltages ($\lambda \geq 420$ nm); Figure S5. Photoelectric conversion efficiency of Bi_2WO_6 NAs, NiFe-LDH/Bi_2WO_6 NAs, Ti_3C_2/Bi_2WO_6 NAs, and NiFe-LDH/Ti_3C_2/Bi_2WO_6 NAs.

Author Contributions: Conceptualization, L.L. and J.Z.; methodology, R.L.; software, R.L..; validation, Y.W. (Yuting Wang) and R.L.; formal analysis, Y.W. (Yuting Wang); investigation, Y.W. (Yuting Wang) and R.L.; resources, W.H.; data curation, R.L. and Y.W. (Yuting Wang); writing—original draft preparation, Y.W. (Yuting Wang) and R.L.; writing—review and editing, Y.W. (Yuting Wang); visualization, Y.W. (Yuting Wang); supervision, Y.W. (Yajun Wang); project administration, Y.W. (Yajun Wang); funding acquisition, Y.W. (Yajun Wang) and Y.W. (Yuting Wang). All authors have read and agreed to the published version of the manuscript.

Funding: This work is supported by the National Key Research and Development Program of China (2021YFB4000405, 2019YFC1904500), National Natural Science Foundation of China (52270115, 52236003, 52203132, 21777080)

Data Availability Statement: Data supporting the findings of this study are available from the corresponding author upon reasonable request.

Conflicts of Interest: The authors declare no conflict of interest.

References

1. Fan, G.; Yang, S.; Du, B.; Luo, J.; Lin, X.; Li, X. Sono-photo hybrid process for the synergistic degradation of levofloxacin by $FeVO_4$/$BiVO_4$: Mechanisms and kinetics. *Environ. Res.* **2022**, *204*, 112032. [CrossRef]
2. Shen, R.; He, K.; Zhang, A.; Li, N.; Ng, Y.H.; Zhang, P.; Hu, J.; Li, X. In-situ construction of metallic Ni_3C@Ni core-shell cocatalysts over g-C_3N_4 nanosheets for shell-thickness-dependent photocatalytic H_2 production. *Appl. Catal. B-Environ.* **2021**, *291*, 120104. [CrossRef]
3. Fei, T.; Yu, L.; Liu, Z.; Song, Y.; Xu, F.; Mo, Z.; Liu, C.; Deng, J.; Ji, H.; Cheng, M.; et al. Graphene quantum dots modified flower like Bi_2WO_6 for enhanced photocatalytic nitrogen fixation. *J. Colloid Interface Sci.* **2019**, *557*, 498–505. [CrossRef]
4. Zhang, Z.; Wang, W.; Yin, W.; Shang, M.; Wang, L.; Sun, S. Inducing photocatalysis by visible light beyond the absorption edge: Effect of upconversion agent on the photocatalytic activity of Bi_2WO_6. *Appl. Catal. B-Environ.* **2010**, *101*, 68–73. [CrossRef]

5. Ren, G.M.; Han, H.T.; Wang, Y.X.; Liu, S.T.; Zhao, J.Y.; Meng, X.C.; Li, Z.Z. Recent Advances of Photocatalytic Application in Water Treatment: A Review. *Nanomaterials* **2021**, *11*, 1804. [CrossRef]
6. Bessy, T.C.; Bindhu, M.R.; Johnson, J.; Chen, S.-M.; Chen, T.-W.; Almaary, K.S. UV light assisted photocatalytic degradation of textile waste water by $Mg_{0.8-x}Zn_xFe_2O_4$ synthesized by combustion method and in-vitro antimicrobial activities. *Environ. Res.* **2022**, *204*, 111917. [CrossRef]
7. Wu, S.J.; Sun, J.G.; Li, Q.; Hood, Z.D.; Yang, S.; Su, T.M.; Peng, R.; Wu, Z.; Sun, W.W.; Kent, P.R.C.; et al. Effects of Surface Terminations of 2D Bi_2WO_6 on Photocatalytic Hydrogen Evolution from Water Splitting. *Acs Appl. Mater. Interfaces* **2020**, *12*, 20067–20074. [CrossRef] [PubMed]
8. Kaur, A.; Sharma, S.; Sood, S.; Umar, A.; Bhinder, S.S.; Kansan, S.K. Visible Light Driven Photo-Catalytic Degradation of Fluoroquinolone Antibiotic Drug Using Bi_2WO_6 Spheres Composed of Fluffy Nanosheets. *Nanosci. Nanotechnol. Lett.* **2016**, *8*, 660–666. [CrossRef]
9. Qi, S.; Zhang, R.; Zhang, Y.; Liu, X.; Xu, H. Preparation and photocatalytic properties of Bi_2WO_6/g-C_3N_4. *Inorg. Chem. Commun.* **2021**, *132*, 108761. [CrossRef]
10. Nguyen Dang, P.; Luc Huy, H.; Guo, P.-C.; Chen, X.-B.; Chou, W.C. Study of photocatalytic activities of Bi_2WO_6/$BiVO_4$ nanocomposites. *J. Sol-Gel Sci. Technol.* **2017**, *83*, 640–646. [CrossRef]
11. Bai, J.; Ren, X.; Chen, X.; Lu, P.; Fu, M. Oxygen Vacancy-Enhanced Ultrathin Bi_2O_3-Bi_2WO_6 Nanosheets' Photocatalytic Performances under Visible Light Irradiation. *Langmuir* **2021**, *37*, 5049–5058. [CrossRef]
12. Li, Z.S.; Luo, M.H.; Li, B.L.; Lin, Q.C.; Liao, X.C.; Yu, H.Q.; Yu, C.L. 3-D hierarchical micro/nano-structures of porous Bi_2WO_6: Controlled hydrothermal synthesis and enhanced photocatalytic performances. *Microporous Mesoporous Mater.* **2021**, *313*, 110830. [CrossRef]
13. Cao, P.F.; Ma, S.Y.; Xu, X.L. Novel ultra-sensitive dandelion-like Bi_2WO_6 nanostructures for ethylene glycol sensing application. *Vacuum* **2020**, *181*, 109748. [CrossRef]
14. Lu, Y.; Zhao, K.; Zhao, Y.H.; Zhu, S.Y.; Yuan, X.; Huo, M.X.; Zhang, Y.; Qiu, Y. Bi_2WO_6/TiO_2/Pt nanojunction system: A UV-vis light responsive photocatalyst with high photocatalytic performance. *Colloids Surf. A-Physicochem. Eng. Asp.* **2015**, *481*, 252–260. [CrossRef]
15. Chen, X.; Chen, C.; Zang, J. Bi2MoO6 nanoflower-like microsphere photocatalyst modified by boron-doped carbon quantum dots: Improving the photocatalytic degradation performance of BPA in all directions. *J. Alloys Compd.* **2023**, *962*, 171167. [CrossRef]
16. Zhang, C.; Zhu, Y.F. Synthesis of square Bi_2WO_6 nanoplates as high-activity visible-light-driven photocatalysts. *Chem. Mater.* **2005**, *17*, 3537–3545. [CrossRef]
17. Cao, S.W.; Shen, B.J.; Tong, T.; Fu, J.W.; Yu, J.G. 2D/2D Heterojunction of Ultrathin MXene/Bi_2WO_6 Nanosheets for Improved Photocatalytic CO_2 Reduction. *Adv. Funct. Mater.* **2018**, *28*, 1800136. [CrossRef]
18. Ali, B.; Abdelkader, E.; Naceur, B.; Houcined, C.; Nadjia, L.; Nourredine, B. Sunlight-driven photocatalytic degradation of Rhodamine B by BiOCl and TiO_2 deposited on NiCr-LDH. *Int. J. Environ. Anal. Chem.* **2021**, *103*, 6722–6741. [CrossRef]
19. He, Y.; Zhou, S.; Wang, Y.; Jiang, G.; Jiao, F. Fabrication of g-C_3N_4@NiFe-LDH heterostructured nanocomposites for highly efficient photocatalytic removal of rhodamine B. *J. Mater. Sci.-Mater. Electron.* **2021**, *32*, 21880–21896. [CrossRef]
20. Suppaso, C.; Pongkan, N.; Intachai, S.; Ogawa, M.; Khaorapapong, N. Magnetically recoverable beta-$Ni(OH)_2$/gamma-Fe_2O_3/NiFe-LDH composites; isotherm, thermodynamic and kinetic studies of synthetic dye adsorption and photocatalytic activity. *Appl. Clay Sci.* **2021**, *213*, 106115. [CrossRef]
21. Wang, R.; Su, S.; Ren, X.; Guo, W. Polyoxometalate intercalated La-doped NiFe-LDH for efficient removal of tetracycline via peroxymonosulfate activation. *Sep. Purif. Technol.* **2021**, *274*, 119113. [CrossRef]
22. Zhang, D.; Dong, W.; Liu, Y.; Gu, X.; Yang, T.; Hong, Q.; Li, D.; Zhang, D.; Zhou, H.; Huang, H.; et al. Ag-In-Zn-S Quantum Dot-Dominated Interface Kinetics in Ag-In-Zn-S/NiFe LDH Composites toward Efficient Photoassisted Electrocatalytic Water Splitting. *Acs Appl. Mater. Interfaces* **2021**, *13*, 42125–42137. [CrossRef] [PubMed]
23. Zhu, Y.; Ren, J.; Yang, X.; Chang, G.; Bu, Y.; Wei, G.; Han, W.; Yang, D. Interface engineering of 3D $BiVO_4$/Fe-based layered double hydroxide core/shell nanostructures for boosting photoelectrochemical water oxidation. *J. Mater. Chem. A* **2017**, *5*, 9952–9959. [CrossRef]
24. Aboubakr, A.E.A.; El Rouby, W.M.A.; Khan, M.D.; Farghali, A.A.; Revaprasadu, N. ZnCr-CO_3 LDH/ruptured tubular g-C_3N_4 composite with increased specific surface area for enhanced photoelectrochemical water splitting. *Appl. Surf. Sci.* **2020**, *508*, 145100. [CrossRef]
25. Chen, S.; Liu, R.; Kuai, Z.; Li, X.; Lian, S.; Jiang, D.; Tang, J.; Li, L.; Wu, R.; Peng, C. Facile synthesis of a novel $BaSnO_3$/MXene nanocomposite by electrostatic self-assembly for efficient photodegradation of 4-nitrophenol. *Environ. Res.* **2022**, *204*, 111949. [CrossRef] [PubMed]
26. Zhao, W.J.; Qin, J.Z.; Yin, Z.F.; Hu, X.; Liu, B.J. 2D MXenes for Photocatalysis. *Prog. Chem.* **2019**, *31*, 1729–1736.
27. Adomavičiūtė-Grabusovė, S.; Ramanavičius, S.; Popov, A.; Šablinskas, V.; Gogotsi, O.; Ramanavičius, A. Selective Enhancement of SERS Spectral Bands of Salicylic Acid Adsorbate on 2D Ti3C2Tx-Based MXene Film. *Chemosensors* **2021**, *9*, 223. [CrossRef]
28. Ran, J.; Gao, G.; Li, F.-T.; Ma, T.-Y.; Du, A.; Qiao, S.-Z. Ti_3C_2 MXene co-catalyst on metal sulfide photo-absorbers for enhanced visible-light photocatalytic hydrogen production. *Nat. Commun.* **2017**, *8*, 13907. [CrossRef]

29. Pasupuleti, K.S.; Thomas, A.M.; Vidyasagar, D.; Rao, V.N.; Yoon, S.G.; Kim, Y.-H.; Kim, S.-G.; Kim, M.-D. ZnO@Ti3C2Tx MXene Hybrid Composite-Based Schottky-Barrier-Coated SAW Sensor for Effective Detection of Sub-ppb-Level NH_3 at Room Temperature under UV Illumination. *ACS Mater. Lett.* **2023**, *5*, 2739–2746. [CrossRef]
30. Mahar, I.; Memon, F.H.; Lee, J.-W.; Kim, K.H.; Ahmed, R.; Soomro, F.; Rehman, F.; Memon, A.A.; Thebo, K.H.; Choi, K.H. Two-Dimensional Transition Metal Carbides and Nitrides (MXenes) for Water Purification and Antibacterial Applications. *Membranes* **2021**, *11*, 869. [CrossRef]
31. Huang, K.L.; Li, C.H.; Li, H.Z.; Ren, G.M.; Wang, L.; Wang, W.T.; Meng, X.C. Photocatalytic Applications of Two-Dimensional Ti_3C_2 MXenes: A Review. *Acs Appl. Nano Mater.* **2020**, *3*, 9581–9603. [CrossRef]
32. Huang, Z.; Zhai, H.; Li, M.; Liu, X. Effects of Ti_3AlC_2 Content on Cu/Ti_3AlC_2 Composites by Hot Pressing Method. *Rare Met. Mater. Eng.* **2011**, *40*, 529–532.
33. Zhang, G.; Hu, Z.; Sun, M.; Liu, Y.; Liu, L.; Liu, H.; Huang, C.-P.; Qu, J.; Li, J. Formation of Bi_2WO_6 Bipyramids with Vacancy Pairs for Enhanced Solar-Driven Photoactivity. *Adv. Funct. Mater.* **2015**, *25*, 3726–3734. [CrossRef]
34. Yang, C.; Huang, Y.; Li, T.; Li, F. Bi_2WO_6 Nanosheets Synthesized by a Hydrothermal Method: Photocatalytic Activity Driven by Visible Light and the Superhydrophobic Property with Water Adhesion. *Eur. J. Inorg. Chem.* **2015**, *2015*, 2560–2564. [CrossRef]
35. Song, X.C.; Zhou, H.; Huang, W.Z.; Wang, L.; Zheng, Y.F. Enhanced Photocatalytic Activity of Nano-Bi_2WO_6 by Tin Doping. *Curr. Nanosci.* **2015**, *11*, 627–632. [CrossRef]
36. Lv, H.; Liu, Y.; Hu, J.; Li, Z.; Lu, Y. Ionic liquid-assisted hydrothermal synthesis of Bi_2WO_6-reduced graphene oxide composites with enhanced photocatalytic activity. *Rsc Adv.* **2014**, *4*, 63238–63245. [CrossRef]